Retention of rising oil droplets in density stratification

Tracy L. Mandel[1,2]†, De Zhen Zhou[1,2], Lindsay Waldrop[3], Maxime Theillard[1], Dustin Kleckner[2], and Shilpa Khatri[1]

[1]Department of Applied Mathematics, University of California, Merced, CA 95343, USA,
[2]Department of Physics, University of California, Merced, CA 95343, USA,
[3]Department of Biological Sciences, Chapman University, Orange, CA 92866

(Received xx; revised xx; accepted xx)

Following the Deepwater Horizon oil well leak in 2010, approximately 40 percent of the spilled oil remained trapped deep beneath the ocean surface. While it has been demonstrated that these trapped intrusion layers, composed of small oil droplets, are caused by interactions with the oceanic density gradient, the exact dynamics underlying the residence time of the oil in these layers is not well understood. In this study, we present results from experiments on the retention of single oil droplets rising through a two-layer density stratification. We track the motion of droplets as they rise through the water column, and delineate two timescales: an entrainment time, and a retention time. The entrainment time is a measure of the time that an oil droplet spends below its upper-layer terminal velocity and relates to the time over which the droplet entrains denser fluid. The retention time is a measure of the time that the droplet is delayed from reaching an upper threshold far from the density transition. The retention time relates to the entrainment time, as well as to the magnitude of the drop's slowdown. These two timescales are found to strongly depend on the Froude number of the system. We find that both timescales are only significantly large for $\mathrm{Fr} \lesssim 1$, indicating that trapping dynamics arise from a balance between drop inertia and buoyancy. We discuss the implications of these findings on the scale of oceanic oil spills, and propose that the size of the bulk plume of oil droplets may be the relevant length scale for trapping in that scenario.

Key words: stratified flows, drops, wakes, ocean processes

1. Introduction

During the Deepwater Horizon oil spill in 2010, about five million barrels of petroleum were discharged 1,500 meters below sea level from the Macondo Well into the Gulf of Mexico (McNutt *et al.* 2012). Oceanographic studies have estimated that approximately two million barrels were trapped in the deep sea, primarily in intrusion layers found at depths between 900 and 1,300 meters (Camilli *et al.* 2010; Kessler *et al.* 2011). These intrusion layers were comprised of very small oil droplets, along with dissolved oil and gas, entrained seawater, and dispersants (Gros *et al.* 2017). While the trapping process and formation of intrusion layers remain poorly understood, it has been demonstrated that these trapped intrusion layers are caused by the interaction of a multiphase oil plume

† Email address for correspondence: tmandel2@ucmerced.edu

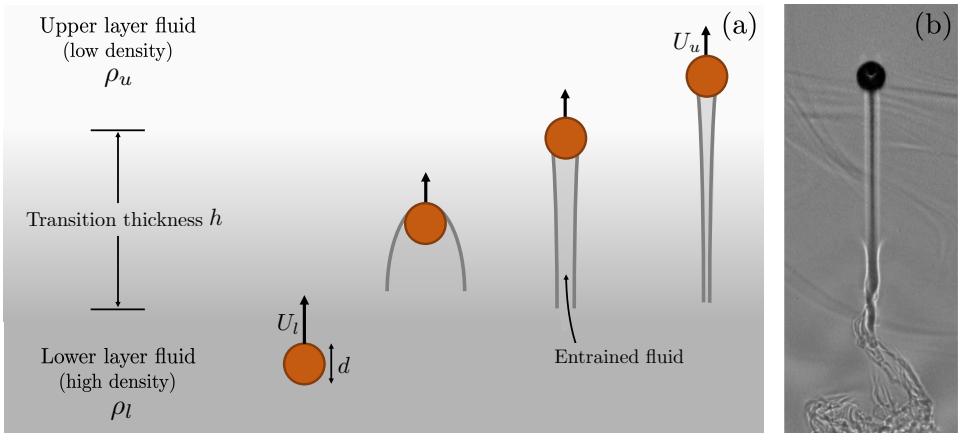

Figure 1: (a) Schematic of a single droplet rising through the transition between two homogeneous-density layers. The droplet entrains denser fluid, decreasing its effective buoyancy as it enters the low density fluid. (b) Shadowgraph image of actual experiment showing the column of entrained fluid being dragged upward by the droplet.

and the inherent oceanic density gradient (Socolofsky & Adams 2002, 2005; Gros *et al.* 2017).

Prior work on rising two-phase plumes, composed of bubbles and oil droplets, has found that in density stratification, the height at which a plume gets trapped is a function of the ambient density gradient, the kinematic buoyancy flux of the plume, and the terminal rise velocity of individual bubbles (Socolofsky & Adams 2002). Several other experimental studies (Murphy *et al.* 2016; Seol *et al.* 2009) have observed similar trapping dynamics. Adalsteinsson *et al.* (2011) found that, while it is clear that entrained fluid plays a role in plume intrusion, the residence time of the oil requires an understanding of how many-particle systems interact with stratification.

Dynamics at the scale of a single drop or particle will thus yield important insight into many-particle plume behavior in stratified fluids. Beyond oil spills, the behavior of a droplet or particle in stratification is of interest in many other areas of fluid mechanics, with applications in atmospheric pollution (Turco *et al.* 1990), turbidity currents (Alavian *et al.* 1992), liquid-liquid extraction systems (Wegener *et al.* 2010), and falling leaves (Lam *et al.* 2019). This simplified fundamental problem is challenging in itself, as when a droplet rises it entrains denser fluid with it, altering the effective buoyancy of the droplet and reducing its upward speed (figure 1).

To our knowledge, all work on the rising of droplets in stratified fluids has been numerical in nature. The current study will thus focus on experimental work, to provide an expansion and validation of previous numerical studies. The numerical simulations of Bayareh *et al.* (2013), for example, showed that the drag coefficient of a spherical drop was enhanced in linearly stratified fluids with drop Froude numbers in the range $4 \leqslant \mathrm{Fr} \leqslant 16$ (where Fr is the ratio of the buoyancy timescale to drop motion timescale). Other numerical work has studied two-droplet (Bayareh *et al.* 2016) and swarm-scale (Dabiri *et al.* 2015) interactions among droplets in linear stratification. These works did not involve a sharp transition between two homogeneous-density fluids, so trapping dynamics were not studied. Recent numerical work by Blanchette & Shapiro (2012) has suggested that the dynamics of oil droplets in stratified fluids may have additional complexities, namely Marangoni forces. These authors found that in a sharp transition in

stratification, a drop may either suddenly accelerate through the transition region or be prevented from crossing into the next layer, depending on the relative interfacial tension between the drop and the two layers.

While experimental work on drops is limited, there is significant prior experimental work that has looked at the small-scale dynamics of rigid spheres rising and falling in stratified fluids. The experiments of Srdić-Mitrović *et al.* (1999) studied the gravitational settling of solid particles through a sharp two-layer stratification and found that stratification drag—that is, an increase in the drag coefficient and an associated deceleration occurring with entry into a stratified layer—was significant in only a narrow range of Reynolds number, $1.5 < Re < 15$. Otherwise, experiments at Reynolds numbers outside of this range showed no significant change in drag as particles passed through the interface, instead behaving similarly to a particle in a homogeneous fluid. Abaid *et al.* (2004) also observed a velocity minimum for a sphere passing through a sharp transition between two homogeneous-density fluids, and in some cases reversal of the sphere's motion. Other experiments, including those of Hanazaki *et al.* (2009), Okino *et al.* (2017) and Akiyama *et al.* (2019), have studied the wake of spheres moving vertically in stratification, and have found that varying trailing jet structures emerge and contribute to fluid entrainment and mixing. However, these three studies were conducted in linear stratification, so the effects of a sharp density transition are unknown in these regimes.

Experimental and theoretical studies of settling porous spheres have also predicted increased drag or prolonged retention times at sharp density transitions (Camassa *et al.* 2009, 2010, 2013; Prairie *et al.* 2013; Panah *et al.* 2017), due to either diffusion of lighter fluid into the settling porous particle, or to entrainment of lighter fluid from above. However, most of these studies were limited to the Stokes regime. Similar studies on spheres in linear stratification (Yick *et al.* 2009; Mehaddi *et al.* 2018) were also conducted at very low Reynolds number. Rising oil droplets in the Deepwater Horizon had Reynolds numbers ranging from 5 to 80, depending on estimates of drop diameter and drop velocity (Socolofsky *et al.* 2011; Weber *et al.* 2012), indicating the necessity of studies to be performed at intermediate and higher Reynolds number.

The focus of our literature review and the corresponding work has been the behavior of particles and droplets in stratification. We note that numerous studies have looked at the behavior of spheroids in homogeneous-density fluids, from vortex shedding and wake dynamics from a sphere (e.g. Horowitz & Williamson 2010; Auguste & Magnaudet 2018) to basic statistics such as terminal rise velocity of droplets (e.g. Wegener *et al.* 2010; Bäumler *et al.* 2011; Bertakis *et al.* 2010). We will examine some terminal droplet behavior in the upper and lower homogeneous-density layers, however, the focus of the present work is on drop dynamics at the density transition between the two layers.

The present work aims to quantify and explain the retention of single oil droplets at the transition between two homogeneous-density fluids, particularly in the parameter space relevant to oceanic oil spills. Using laboratory experiments, we examine flow and retention for a range of drop sizes, drop densities, and ambient stratification profiles. We also qualitatively assess fluid entrainment and discuss the implications of these findings for field-scale dynamics. In section 2, we discuss the nondimensional parameters relevant to this problem. In section 3, we will describe the experimental setup and measurements taken. We will discuss our results in section 4, beginning with analysis of the drop's position and velocity, and then introducing two timescales relating to fluid entrainment and droplet retention. We will close with a discussion of the implications of this work and future directions in section 5.

Parameter	Symbol	Definition	Range of values
Drop density	ρ_d	-	0.9375 – 0.9927 g cm^{-3}
Ambient fluid density	ρ_f	-	0.9972 – 1.117 g cm^{-3}
Terminal drop speed	U_f	-	0.33 – 13.3 cm s^{-1}
Drop diameter	d	-	0.15 – 0.78 cm
Transition thickness	h	-	3.0 – 9.0 cm
Buoyancy frequency	N	$\sqrt{-g/\rho_u(\partial\rho/\partial z)}$	3.6 – 7.5 s^{-1}
Dynamic viscosity of water	μ_u	-	0.01 g cm^{-1} s^{-1}
Dynamic viscosity of oil	μ_d	-	0.093 – 0.10 g cm^{-1} s^{-1}
Drop Reynolds number	Re_d	$\rho_d U_u d/\mu_u$	5.4 – 540
Reynolds number	Re_f	$\rho_f U_f d/\mu_u$	5.4 – 1060
Archimedes number	Ar_f	$g(\rho_f-\rho_d)\rho_f d^3/\mu_u^2$	140 – 700,000
Froude number	Fr	$U_u/(Nd)$	0.38 – 4.2
Relative density	$\Delta\rho_u$	$(\rho_u-\rho_d)/\rho_u$	0.0045 – 0.061
Relative layer thickness	-	h/d	4.5 – 52

Table 1: Definition and range of parameters covered in laboratory experiments. Variables with the subscript f represent that quantity in either the upper layer (e.g., ρ_u and U_u) or lower layer (e.g., ρ_l and U_l).

2. Nondimensional parameters

We covered a range of the parameter space relevant to this problem, particularly in the intermediate Reynolds number regime. Table 1 lists the parameter definitions and ranges covered in this study, which spanned 180 different droplet experiments. Non-dimensional parameters with the subscript f, such as Re_f, encompass two separate nondimensional numbers for a single drop's behavior in the upper and lower layers of ambient fluid, Re_u and Re_l. The subscript f in the given definition is thus replaced by the corresponding upper (u) or lower (l) layer quantity. The subscript d represents the corresponding nondimensional number or parameter for the drop fluid properties. In these definitions, ρ represents fluid density, U represents the terminal drop velocity in a given homogeneous-density region, d is the drop diameter, μ is the dynamic viscosity of the fluid, and h is the thickness of the transition region, computed as the height encompassing 95% of the density variation between the upper and lower layers. The buoyancy frequency, N, is defined as $N = \sqrt{-g/\rho_u(\partial\rho/\partial z)}$, where $\partial\rho/\partial z$ is computed as the least-squares slope of a 0.6 cm-wide region in the transition region of the density profile at rest, centered at $z = 0$.

Following the definitions given in table 1, the Reynolds number (Re_f or Re_d) represents the ratio of inertial to viscous forces. The Archimedes number (Ar_f) is the ratio of buoyant forces to viscous forces. The Froude number (Fr) can be thought of in several ways: (1) as the ratio of flow inertia to external gravitational forces; (2) as the ratio of the buoyancy timescale ($1/N$) to the drop motion timescale (d/U_u); or (3) as a ratio of the speeds at which various information about the flow is propagating, i.e. the ratio of droplet speed to an internal wave speed. In experiments, these parameters were varied by changing the drop diameter, the drop density, and the transition region thickness (and thus N).

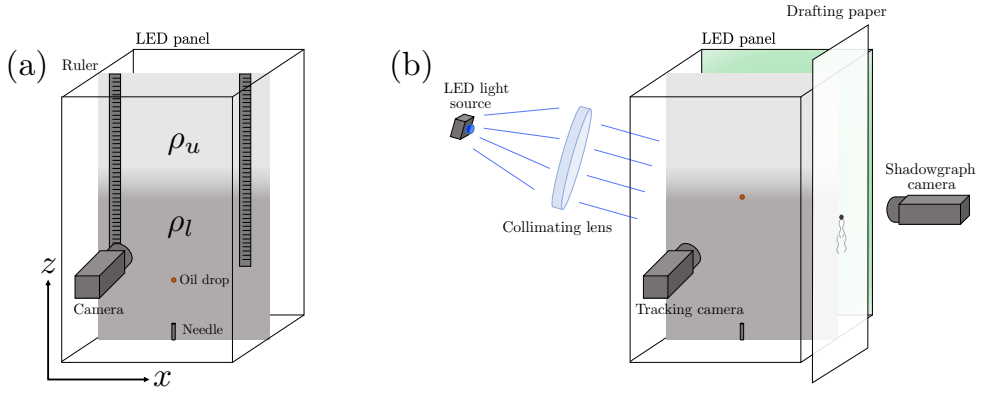

Figure 2: Schematic of experimental setup for (a) tracking drop motion and measuring density profiles and (b) combined shadowgraph-tracking experiments.

3. Experimental approach

3.1. *Experimental setup*

Experiments were conducted in a 61 cm tall acrylic tank with a width and depth of 30.5 cm by 30.5 cm. A schematic of this tank is shown in figure 2(a). NaCl (Morton Canning & Pickling Salt) was used as the stratifying medium. Fluid for the two layers was prepared in two 35-gallon tanks with recirculating pumps, which were filled with reverse osmosis water. Salt was added to one tank and dissolved. Both tanks were left to circulate at room temperature to eliminate convection in the filled experimental tank.

The experimental tank was filled using two methods: (1) a two-layer filling method that yielded error function-type density profiles, and (2) a computer-controlled method, yielding linear density profiles in the transition region. For the first method, the tank was filled first with salt water (ρ_l = 1.106 to 1.117 g/cm^3) and then with fresh water (ρ_u = 0.9972 to 0.9981 g/cm^3), with a sponge float acting as a diffuser to reduce mixing between the two layers. To obtain a thin transition region (3-4 cm), the tank was allowed to sit and diffuse for 2-3 hours, until the optical distortion caused by the difference in refractive indices between the two layers had reduced. To obtain a thicker transition region (7-8 cm), the tank was allowed to diffuse another 18 hours. This two-layer filling method yielded error-function shaped density profiles, as seen in figure 3(a,b). The second filling method allowed more precise control of layer thickness. For this method, two computer-controlled peristaltic pumps (New Era Pump Systems NE-9000) feeding from a fresh water bucket and a salt water bucket were linearly ramped up and down to generate a linear stratification between the upper and lower layers. These could be programmed to yield either a 4cm or 8cm thick transition layer. Examples of such density profiles are shown in figure 3(c,d). The gray region in these density profiles represents the layer thickness h, where 95% of the density variation between the upper and lower layers occurs.

Oil droplets were composed of a mixture of 10 cSt silicone oil (Clearco Products Co.) and halocarbon oil (Sigma Life Science Halocarbon oil 27) in order to study a range of drop densities ρ_d, from 0.9375 to 0.9927 g/cm^3. Oil fluorescent tracer (Risk Reaction DFSB-K175 UV Orange) was also added for contrast. Drops were released individually by dispensing a small amount of oil using a syringe pump or handheld syringe, which fed into a 19 gauge needle inserted through a flange in the base of the tank. A waiting time

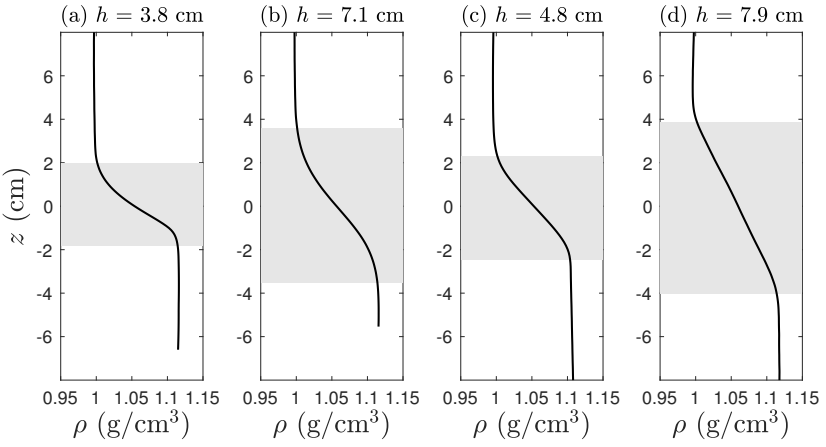

Figure 3: Representative density profiles from experimental realizations for thinner and thicker stratified layers. Profiles were measured using synthetic Schlieren, as described in section 3.2. The gray shading represents the transition region encompassing 95% of the density variation between the upper and lower layers, denoted by the distance h. (a) The stratified layer was generated by filling the two layers directly with a sponge diffuser and then left to diffuse for 3-4 hours. (b) The layer was generated as for (a), then allowed to diffuse for 18 hours. (c,d) The layer was generated using linearly ramping pumps from fresh and salt water reservoirs in order to more precisely control transition thickness.

of at least 15 minutes between drop releases was chosen to ensure the tank was quiescent for each experiment.

3.2. *Experimental measurements*

Physical characteristics of the ambient fluid and oil droplets were measured prior to experiments. An Anton Paar Lovis 2000 ME microviscometer and DMA 4100 M densitometer were used to measure the viscosities and densities of the fresh water, salt water, and droplet fluid. The densitometer also provided direct measurements of the fluid's temperature.

During experiments, images of the injected drops were captured at 120 to 125 fps using a high-speed camera (Photron FASTCAM SA3 at 1 MP, Point Grey Grasshopper3 at 5 MP) aligned with the plane of drop motion. A panel of light emitting diodes (LEDs) was placed behind the tank, along with a diffusive screen of vellum paper between the tank and lights, to increase the contrast between drops and the background. Before each drop was released, an image was taken of the field of view, including a calibration ruler placed in line with the needle and plane of droplet motion. Because of the tank's density stratification, the refractive index encountered by a light ray changes as light passes through the tank. The images captured by the camera thus have refractive distortion. This distortion was corrected by calibrating the drop position relative to the refracted ruler image, as shown in figure 4. In some cases, the drops exhibited slight out-of-plane motion, which we estimate to contribute 1 percent or less error in measured vertical position, based on a camera distance of ~ 1 meter and out-of-plane motion on the order of 1 cm.

Following distortion correction and subtraction of a mean background image, drop position over time was then tracked using the Trackpy software package (Allan *et al.* 2016), which uses center-of-mass detection to determine droplet position. Example tracked paths

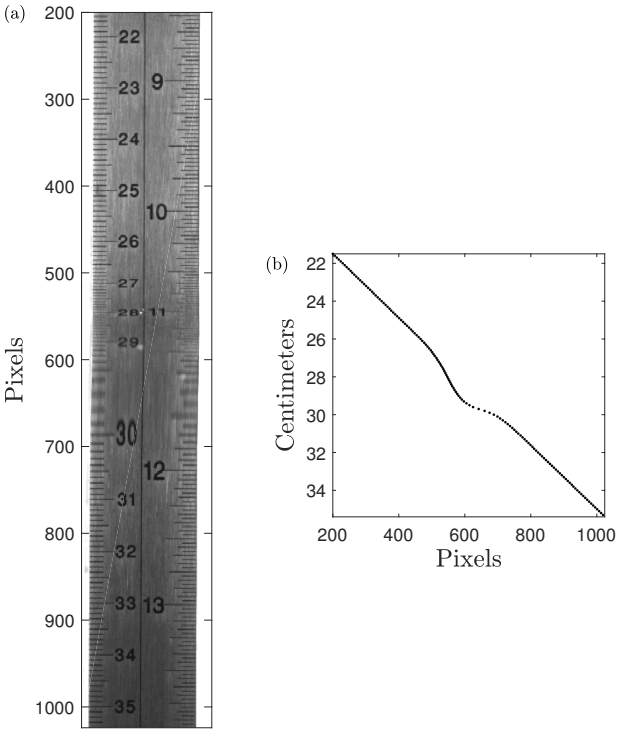

Figure 4: (a) Example ruler image used for remapping images to remove refractive distortion. (b) Plot of centimeter reading on ruler versus pixel location.

and velocities for five drops are shown in figures 5, 6 and 7. Instantaneous velocities were obtained following the methods of Srdić-Mitrović *et al.* (1999), in which a least-squares line was fit to a window of 7 points of vertical position ($\sim$0.06 sec of data) and the best-fit slope was assigned as the velocity of the center point in the window. Upper and lower layer terminal velocities, U_u and U_l, were computed as the least-squares slope of the drop trajectory in regions with constant speed in the upper and lower layers, respectively.

Drop diameters were measured manually from an image in the lower layer, and calibrated from pixels to centimeters. For 145 cases, manually measured and calibrated diameters were verified against images of drops taken using a telecentric lens; telecentric images yielded diameters that varied on average by 0.16 mm from the other method (an average relative difference of less than 5%), giving an estimate of the error in manual measurement and calibration.

In addition to correcting for refractive distortion, the quantified distortion of the ruler was also used to determine density profiles using synthetic Schlieren (Sutherland *et al.* 1999; Dalziel *et al.* 2000). Optical focusing and spreading of ticks on the ruler within the transition region were compared with the even spacing in the upper and lower layers, and the apparent displacement Δz of these ticks was then converted to a density gradient following the assumptions of linearity, two-dimensionality, and small incident ray angles, as described in the above references. The full density profile was obtained by integrating

the gradient from the known upper layer density using the equation below, and resulting in density profiles as shown in figure 3.

$$\rho(z) = \rho_u + \frac{2\rho_u}{g}\frac{1}{\beta L_{ruler}^2}\int_{z_u}^{z} \Delta z \; dz' \tag{3.1}$$

where Δz is the measured apparent displacement field (the difference between the curve shown in figure 4 and vertical height), and $\beta \simeq 1.88$ s^2 cm^{-1} following Sutherland *et al.* (1999). Because precise measurement of the exact distance between the ruler and the tank side wall, L_{ruler}, was difficult, and precision was difficult to maintain from experiment to experiment over 180 diffferent runs, this length was adjusted manually by ± 0.8 cm to yield a profile whose constant upper and lower layer densities matched those measured with the hand-held densitometer.

To visualize the wakes of droplets, shadowgraph experiments were performed. A schematic of this setup is shown in figure 2(b). Polyester drafting film (West Design Polydraw) was placed on one side of the tank, and a camera was placed facing the drafting paper so that drops and their wakes could be visualized via the focusing and defocusing of incoming light rays. A collimated light source (Thorlabs M450LP1 450 nm LED, in conjunction with an Edmund Optics 200 mm diameter, 800 mm focal length PCX condenser lens) was placed on the opposite side of the tank. The LED light source and collimating optics were set to angle downwards at about 30 degrees from the horizontal in order to avoid total internal reflection within the transition region, which would have occluded ~ 1 cm of the droplet's path and also caused oversaturation in images. The images presented here thus show the projected fluid structures viewed at this angle, rather than a perfectly perpendicular view of the $x - y$ plane. A tracking camera was placed perpendicularly to the shadowgraph camera, opposite the LED backlighting panel, which was set to emit green light. Each camera was equipped with a bandpass filter so that illumination from the backlighting panel and the 450 nm LED could be separated. The tracking camera was fitted with a Thorlabs FELH0550 long-pass filter with a cut-on wavelength of 550 nm, and the shadowgraph camera used a Thorlabs FES0500 short-pass filter with a cut-off wavelength of 500 nm. Both tracking and shadowgraph images were synchronized using a function generator (Siglent SDG1025) that triggered the two cameras externally. Before a set of experiments, a calibration image was taken for each camera with a clear acrylic ruler in the field of view; the ruler was then moved to the edge of the tank and the tank allowed to settle for approximately 30 minutes before releasing droplets. Shadowgraph images were post-processed by correcting for optical distortion and then subtracting a background image.

4. Results

We begin by discussing basic properties of the droplet motion. We first demonstrate how droplet position and velocity vary with experimental conditions. We then discuss the terminal velocity of the droplets in the upper and lower layers, as a nondimensional predictor of this behavior is useful for oil spill models. In the last two sections of the results, we analyze the timescales over which fluid entrainment and significant droplet retention occur, discuss their dependence on the nondimensional parameters of the system, and delineate when drops are significantly retained at the transition region. Finally, we connect these timescales to flow visualizations of the droplet's wake.

4.1. *Drop paths and velocities*

Shown in figures 5 and 6 are a sequence of shadowgraph images for (A) a larger (d = 0.40 cm) and (B) a smaller (d = 0.28 cm) droplet, both composed of the densest oil mixture (ρ_d = 0.9927 g/cm^3) and rising through a 4.6 cm transition region. Relative shading indicates variation in the second derivative of density (Settles 2012). As the drops exit the transition region, an internal wave field is generated. Also shown in each figure are the corresponding vertical drop position, z, and velocity, u, as a function of time, t, for each set of shadowgraph images. The droplets slow as they pass through the transition region (snapshots a-c in both sets of shadowgraph images), and reach a velocity minimum (snapshots e-f) just above the top of the transition region. The drop then eventually regains speed (snapshots g-i), asymptoting to its upper-layer terminal velocity U_u, indicated as the dashed grey line in the velocity plots, by about snapshot j. A complex wake structure can also be observed in the shadowgraphs, which will be discussed in detail in section 4.4.

To demonstrate how varying different experimental parameters affect drop motion, figure 7 shows sample drop paths and velocities over time for four example experimental droplet cases. The first case, shown in figure 7(a,e), is the droplet shown in figure 6. We use this small, dense droplet passing through a 4.6 cm transition region as a reference case for comparison with: (b,f) a similarly-sized, lighter droplet in similar ambient stratification; (c,g) a larger, dense droplet in similar stratification; and (d,h) a small, dense droplet passing through a thicker transition region of 7.1 cm. It can be seen that lighter droplets have significantly higher terminal velocities in the upper layer, and that small, dense droplets take significantly longer to traverse the field of view of the camera. The drops in this second case (a,c,d) also remain at a speed lower than their upper layer terminal velocity U_u for an extended period of time, indicating that entrained ambient fluid plays a role in delaying the drop's upward motion. Analysis of these delays will be presented in section 4.3.

4.2. *Terminal velocity*

Droplets reach a constant, terminal velocity in both the upper and lower layers. This terminal velocity appears to be governed by buoyancy, viscosity, and inertia. The drop's Archimedes number in the upper and lower layer is compared to its Reynolds number in each layer in figures 8(a,b). As noted in table 1, the definitions of these two nondimensional numbers is as follows:

$$\mathrm{Ar}_f = g\frac{(\rho_f - \rho_d)\rho_f d^3}{\mu_u^2} \tag{4.1}$$

$$\mathrm{Re}_f = \frac{\rho_f U_f d}{\mu_u} \tag{4.2}$$

where the Archimedes number represents the ratio of buoyant to viscous forces and the Reynolds number represents the ratio of inertial to viscous forces. As before, the subscript f represents either the upper (u) or lower (l) layer property, and U_f represents the terminal drop speed in that corresponding layer. Each drop thus yields two data points of Ar_f and Re_f. Measurements of Ar_l and Re_l are represented as black circles, while values of Ar_u and Re_u are shown as blue triangles.

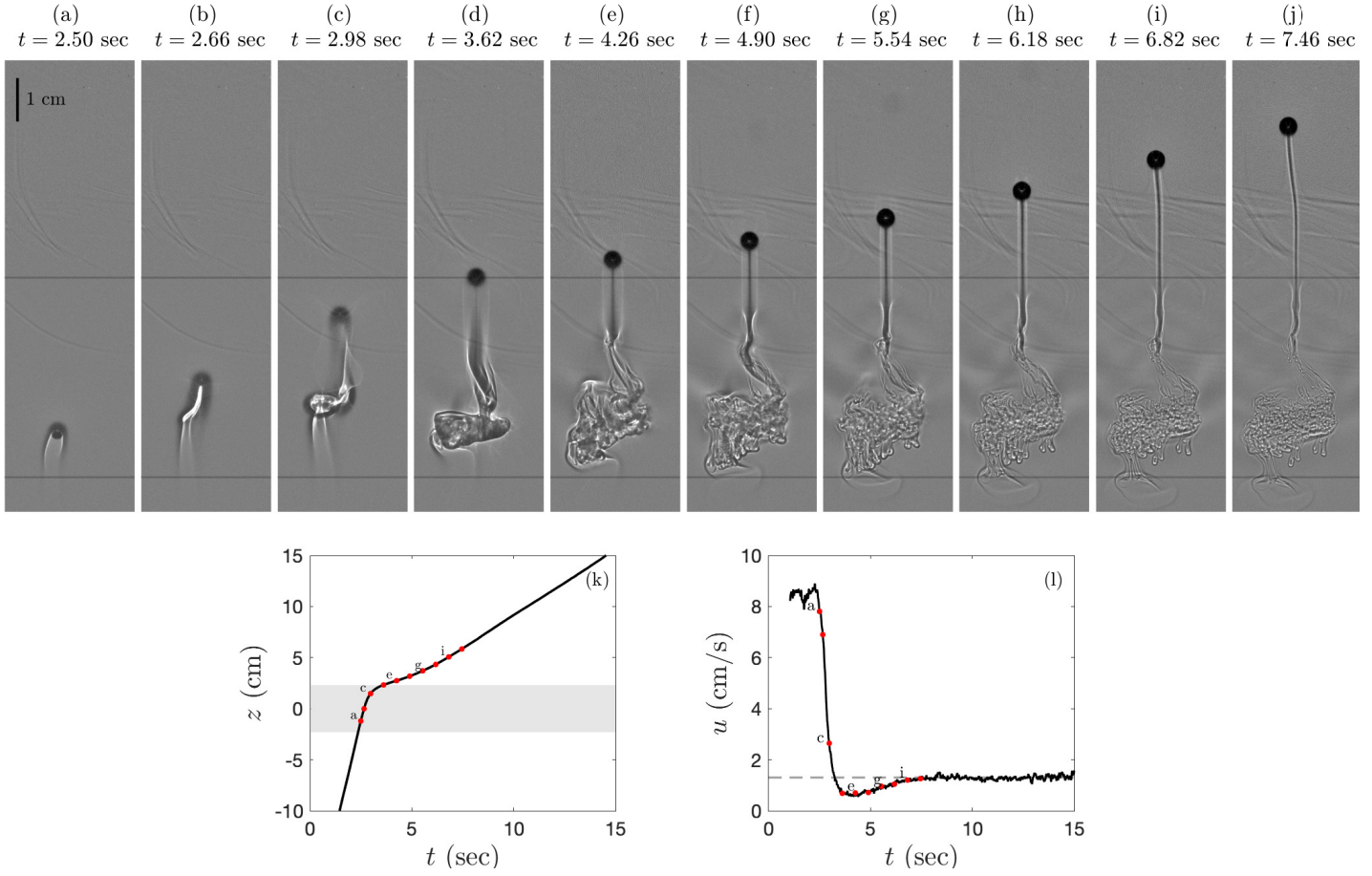

Figure 5: (a-j) Shadowgraph images, case A. For this case, Fr = 0.55, $\Delta\rho_u = 0.0045$, $\mathrm{Re}_l = 370$, $\mathrm{Re}_u = 51.4$, and $h/d = 11.6$. Grey horizontal lines on the images indicate the upper and lower extents of the transition region. (k,l) Tracked position and velocities versus time. Red (·) symbols indicate the location of the shadowgraph snapshots. The grey region in the position versus time graph (k) indicates the extent of the transition region. See Movie 1 online for a video animation of these shadowgraph images.

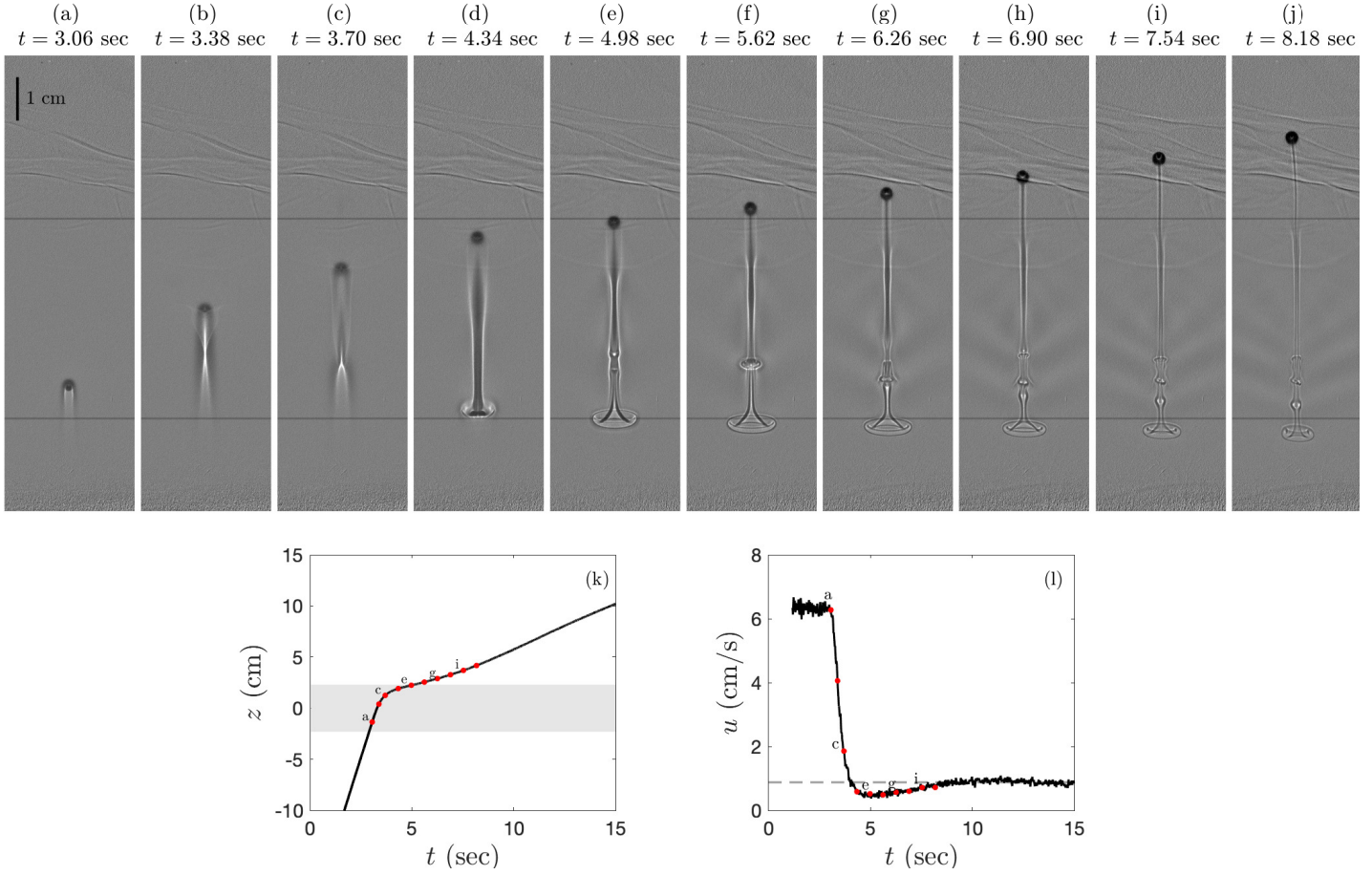

Figure 6: (a-j) Shadowgraph images, case B. For this case, Fr $= 0.53$, $\Delta\rho_u = 0.0045$, $\mathrm{Re}_l = 196$, $\mathrm{Re}_u = 24.6$, and $h/d = 16.4$. See figure 5 for a full description. See Movie 2 online for a video animation of these shadowgraph images.

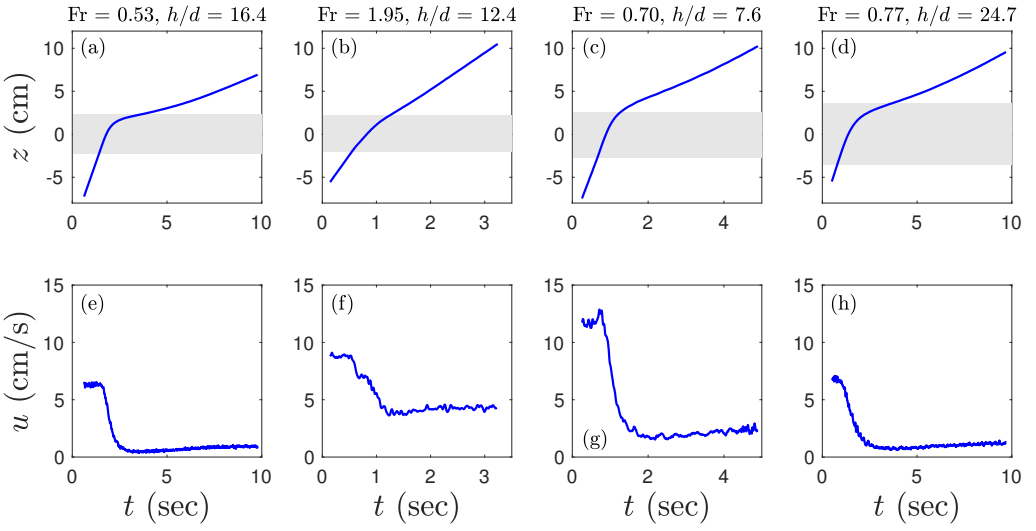

Figure 7: Vertical positions (a-d) and instantaneous velocities (e-h) versus time for four experiments. The shaded area in (a-d) represents the transition region. (a,e) Tracking data from Shadowgraph B: a relatively small, dense reference droplet passing through a 4.6 cm transition region; Fr = 0.53, $\Delta\rho_u$ = 0.0045, Re_l = 196, Re_u = 24.6, h/d = 16.4. (b,f) A less dense droplet; Fr = 1.95, $\Delta\rho_u$ = 0.048, Re_l = 332, Re_u = 145, h/d = 12.4. (c,g) A larger droplet; Fr = 0.70, $\Delta\rho_u$ = 0.0045, Re_l = 882, Re_u = 181, h/d = 7.6. (d,h) A small, dense droplet passing through a 7.1 cm transition region; Fr = 0.77, $\Delta\rho_u$ = 0.0054, Re_l = 220, Re_u = 32.3, h/d = 24.7.

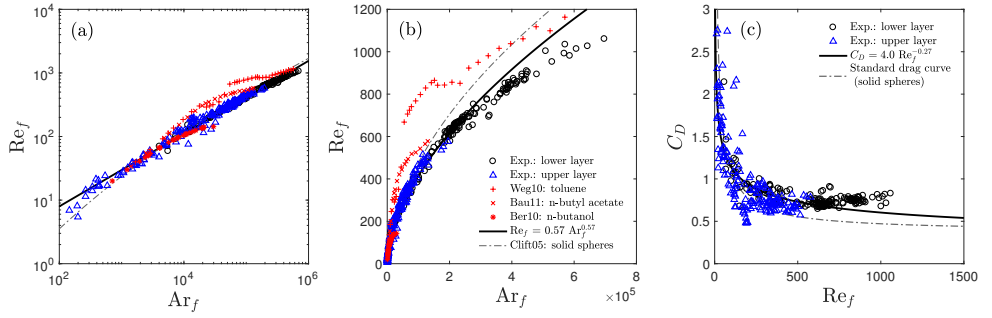

Figure 8: Reynolds number versus Archimedes number for terminal drop behavior in the upper and lower layers, shown on (a) logarithmic and (b) linear scale. (a,b) Experimental data from this study are shown as black circles and blue triangles. A power law relationship was fit to these experimental data, with R^2 = 0.99, shown as the solid black line. Also plotted are terminal velocity data from studies with other droplets of varying interfacial tension in water (Wegener *et al.* 2010; Bäumler *et al.* 2011; Bertakis *et al.* 2010), represented by red markers. The empirical equation for the terminal velocity of solid spheres from Clift *et al.* (2005) is shown as the grey dot-dashed line. (c) Drag coefficient in the upper and lower homogeneous layers. A best-fit to the data is $C_D = 4.0\mathrm{Re}_f^{-0.27}$, with $R^2 = 0.66$. Observed drag coefficients at higher Reynolds number are generally higher than the standard drag curve for solid spheres.

A power-law fit was found to describe the relationship between these two parameters from experimental measurements:

$$\mathrm{Re}_f = 0.57\mathrm{Ar}_f^{0.57} \tag{4.3}$$

with $R^2 = 0.99$. This compares reasonably well with the relationship given by Clift *et al.* (2005) for the range $435 < \mathrm{Ar} \leqslant 1.16 \times 10^7$ and $12.2 < \mathrm{Re} \leqslant 6.35 \times 10^3$,

$$\log_{10} \mathrm{Re} = -1.81391 + 1.34671W - 0.12427W^2 + 0.006344W^3, \tag{4.4}$$

where $W = \log_{10}(4/3\mathrm{Ar})$, shown as the dot-dashed line in figures 8(a,b). It should be noted that this empirical equation for terminal velocity is for a solid sphere, not a deformable liquid drop.

Also shown in figures 8(a,b) are terminal velocities from experiments and numerical simulations of drops rising in homogeneous-density water from several other studies with varying Morton number. The Morton number ($\mathrm{Mo} = g\mu_u^4(\rho_f - \rho_d)/(\rho_f^2\gamma^3)$) describes the importance of gravity and viscosity relative to interfacial tension γ and inertia, and is used to characterize the shape of drops and bubbles. Shown are velocities from Wegener *et al.* (2010) for toluene droplets ($\mathrm{Mo} = 1.95 \times 10^{-11}$), Bäumler *et al.* (2011) for *n*-butanol acetate droplets ($\mathrm{Mo} = 2.87 \times 10^{-10}$), and Bertakis *et al.* (2010) for n-butanol droplets ($\mathrm{Mo} = 1.23 \times 10^{-6}$). For some of these cases in the literature, the drop aspect ratio (the ratio of vertical drop diameter to horizontal drop diameter) was much less than 1 due to a higher Morton number, which explains some of the divergence from our experimental data, which we estimate to have a Morton number on the order of 10^{-11} to 10^{-12}. Although there exist many more studies that compute a terminal velocity relation for droplets or nonspherical solids in homogeneous fluid (e.g. Wallis 1974; Ganguly 1990), the majority are for low Reynolds number flows and not applicable here.

Figure 8(c) also shows the approximate drag coefficient of drops in each homogeneous-density layer, computed as

$$C_D = \frac{4}{3}\frac{g(\rho_f - \rho_d)d}{\rho_f U_f^2} \tag{4.5}$$

following Clift *et al.* (2005). The observed drag coefficient tends to be higher than that predicted by the standard drag curve (Clift *et al.* 2005, see e.g. Table 5.2).

In summary, for drops in the parameter space studied here, if the viscosity and density of the ambient fluid, as well as density and diameter of the drop are known, then the drop's terminal speed can be predicted with reasonable accuracy using the relation given in equation 4.3.

4.3. *Entrainment and retention timescales*

As shown in figures 5, 6, and 7, some droplets experienced a significant slowdown as they passed through the transition region. This slowdown is in part due to the entrainment of denser fluid. It is thus useful to look at metrics of drop retention that measure both the length of time that fluid is entrained, as well as the length of time that the drop is physically retained in the transition layer.

We will consider the first metric to be the entrainment time, t_e. This timescale is demonstrated in figure 9, using both vertical drop position and drop velocity. The entrainment time measures the amount of time the drop spends below its upper layer terminal velocity U_u. It is computed as the time between when the drop first slows to U_u, and when the drop again speeds up to this same velocity. The point where the drop has

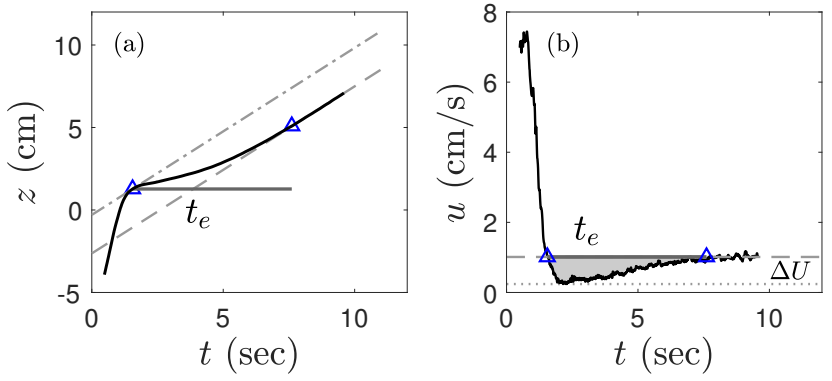

Figure 9: Definition of drop entrainment time, t_e, using (a) vertical drop position and (b) drop velocity. The black line represents the experimental measurement. The grey dashed line shows U_u, either as (a) the slope of the position or (b) as a velocity threshold. The grey dot-dashed line in (a) is a tangent line with a slope of U_u, used to find the point where the drop's velocity first reaches this value. In our definition, the entrainment time is the length of time that the drop's velocity is less than the upper layer terminal speed. It is computed as the time between when the drop first slows to U_u (first blue triangle in both figures) and when the drop again speeds up to this velocity (second blue triangle in both figures). The point where the drop has asymptotically reached its upper-layer velocity is chosen as the point at which the Euclidean distance between the drop position, represented by the black line in (a), and the grey dashed line in (a) is less than 5% of the drop diameter. The difference ΔU between the minimum velocity $U_{\min}$ and U_u is shown in (b).

asymptotically reached U_u again is chosen as the point at which the distance between the drop position (the black line in figure 9(a)) and a line representing the upper layer terminal speed (the grey dashed line in figure 9(a)) is less than 5 percent of the drop diameter. This timescale is very similar to the delayed settling time (DST) used in Prairie *et al.* (2013).

The second metric is a retention time, t_r, the time that the droplet is retained in the transition layer. This time is shown in figure 10(a), and is computed as the time between when the drop actually passes an upper threshold ($z \approx 10$ cm, where $z = 0$ is the center of the transition region), and when it would have passed the upper threshold if it had not slowed down once it first reached U_u. Figure 10(b) compares values of t_e and t_r, which follow a power-law relationship of $t_r = 0.080 t_e^{1.7}$ with an R^2 value of 0.92. There is obviously a strong relationship between these two metrics, with droplets that have a long entrainment timescale also being retained the longest.

The retention time can also be expressed in terms of a retention distance d_r and the upper layer terminal velocity:

$$t_r = \frac{d_r}{U_u} \tag{4.6}$$

and d_r can be scaled as

$$d_r \sim t_e \Delta U, \tag{4.7}$$

where $\Delta U = U_u - U_{\min}$ (figure 9(b)). We found a best-fit relation of $d_r = 0.46 t_e \Delta U$, with

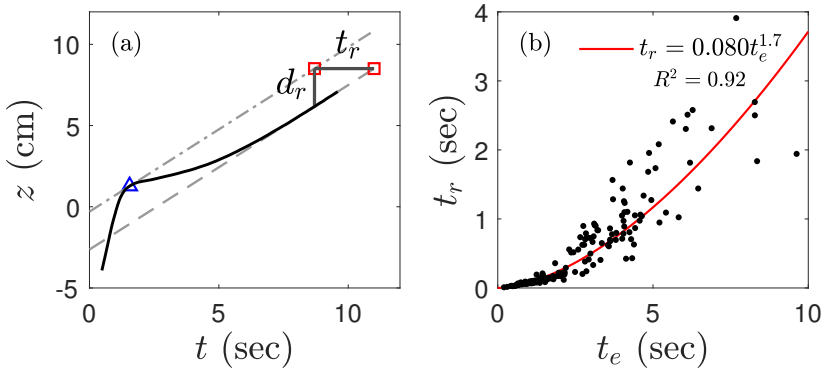

Figure 10: (a) Definition of drop retention time t_r. t_r is computed as the time between when the drop actually passes an upper threshold, and when it would pass the upper threshold if it hadn't slowed down further after it first slowed to U_u (i.e., if the drop had instead followed the dot-dashed path after the blue triangle). The retention distance d_r is also shown. (b) Comparison of t_r with t_e. The best-fit power law is $t_r = 0.080t_e^{1.7}$ with $R^2 = 0.92$.

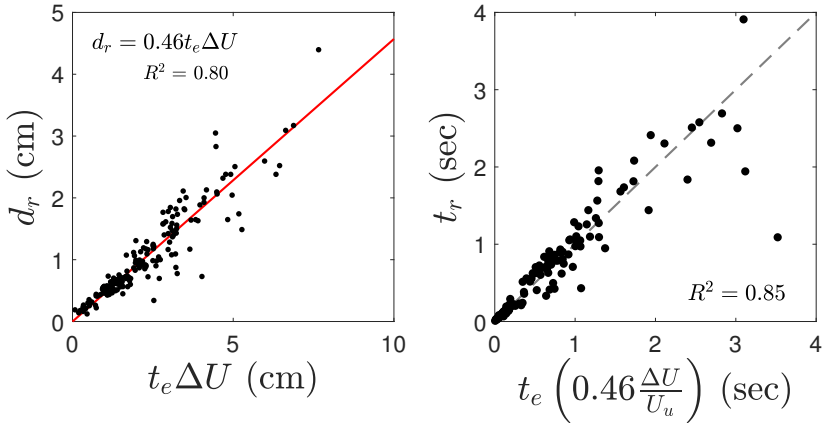

Figure 11: (a) Best-fit for the relationship in equation 4.7, $d_r = 0.46t_e\Delta U$, with $R^2 = 0.80$. (b) Equation 4.8, with a coefficient of determination of 0.85. The dashed grey line indicates a 1:1 relationship.

an R^2 value of 0.80, as shown in figure 11(a). This expression can then be substituted into equation 4.6, yielding

$$t_r = t_e\left(0.46\frac{\Delta U}{U_u}\right). \tag{4.8}$$

The retention time is, therefore, the entrainment time multiplied by a constant, $c = 0.46$, and by a factor representing the relative magnitude of the drop's slowdown, $\Delta U/U_u$. This relationship is shown in figure 11(b), with an R^2 value of 0.85. The physical retention of a drop at the transition region is thus a function of the length of time that denser fluid is appreciably entrained (t_e), and of the amount of denser fluid that is entrained, represented by the relative drop slowdown $\Delta U/U_u$.

In order to understand how environmental conditions affect these timescales, the

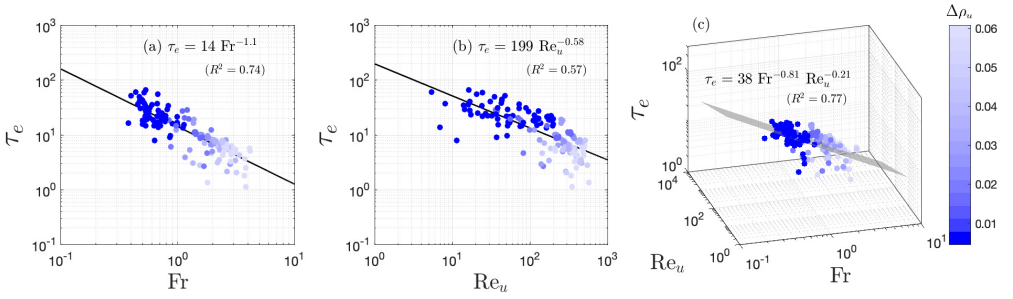

Figure 12: Nondimensional drop entrainment time, τ_e, versus Fr and Re_u. Shading indicates the drop's relative density to the upper layer, $\Delta\rho_u$. The goodness of fit is only marginally improved by incorporating both Fr and Re_u, rather than simply Fr.

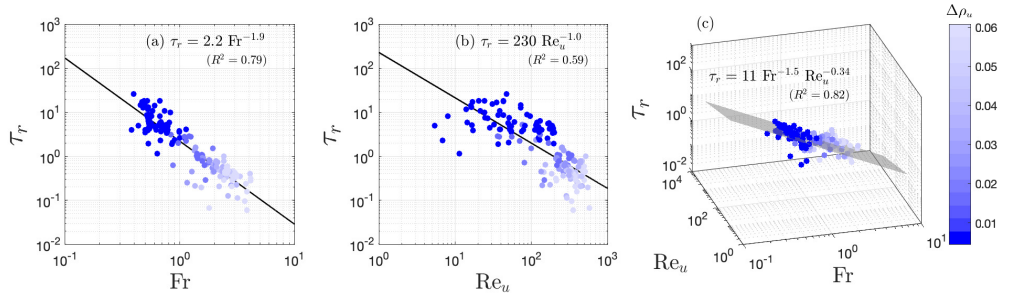

Figure 13: Nondimensional drop retention time, τ_r, versus Fr and Re_u. Shading indicates the drop's relative density to the upper layer, $\Delta\rho_u$. As in figure 12, the goodness of fit is only marginally improved by incorporating Re_u as well as Fr.

retention and entrainment times were then compared against nondimensional parameters governing the drop's rise. Figures 12 and 13 show nondimensional entrainment time, $\tau_e = t_e N$, and nondimensional retention time, $\tau_r = t_r N$, as a function of Froude number and Reynolds number. These timescales are more strongly correlated with the Froude number, indicating the importance of stratification in drop retention. Incorporating both variables to predict timescales, i.e. as a function of both Fr and Re_u, yields only marginal improvement in the goodness of fit. We therefore conclude that the drop Froude number is adequate to characterize entrainment and retention dynamics. Other nondimensional numbers, including Re_l, h/d, and a lower-layer Froude number, were also compared but did not yield significant collapse of the data and so are not presented here.

Nondimensional entrainment and retention times are plotted against Fr alone in figure 14. As shown in figures 12 and 13, both time metrics have a power law relationship with Froude number, with larger nondimensional retention times occurring for small Fr. A delineation can be drawn at $\mathrm{Fr} = 1$. For $\mathrm{Fr} \geqslant 1$, drop motion is happening on a timescale smaller than the buoyancy timescale, and the drop behaves as if it were in a homogeneous fluid; retention times are close to zero. However, for $\mathrm{Fr} < 1$, significant drop retention is observed. As the buoyancy timescale $(1/N)$ becomes less than the drop timescale (d/U_u), the drop is more significantly retained in the transition region. This correlates to buoyancy forces being important and strong enough to counter the drop's inertial forces. Conceptually, one may also consider that for $\mathrm{Fr} < 1$, the drop's velocity is less than a characteristic internal wave velocity, Nd, and the drop does not have the kinetic energy required to "punch through" the transition region.

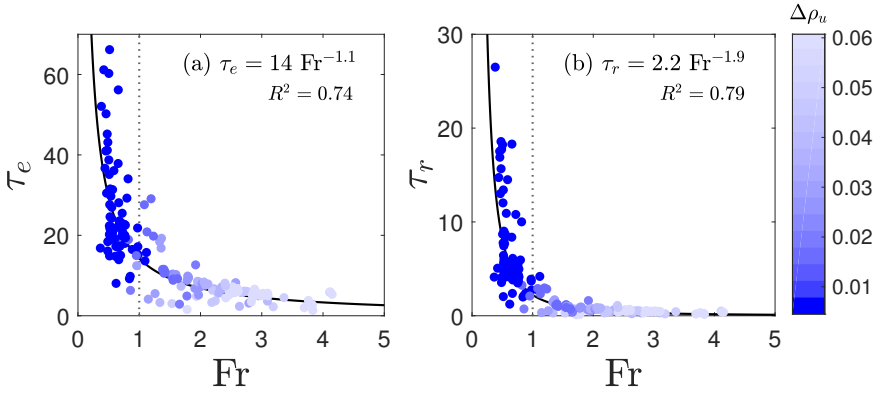

Figure 14: Nondimensional retention and entrainment times versus Froude number. Shading indicates the drop's relative density to the upper layer. Best-fit power laws are shown as the black line in (a) and (b). In (a), $\tau_e = 14\mathrm{Fr}^{-1.1}$, with $R^2 = 0.74$. In (b), $\tau_r = 2.2\mathrm{Fr}^{-1.9}$, with $R^2 = 0.79$.

4.4. *Fluid entrainment*

Above, we have given a conceptual model of how fluid entrainment ultimately affects the retention time. Here, we discuss visualizations of the wakes of the droplets first shown in 4.1, and how the diameter of the tail of fluid dragged by the drop relates to the entrainment timescale. This will in turn impact the retention time via equation 4.8, as discussed in section 4.3.

Shown in figures 5 and 6 were a sequence of shadowgraph images for (A) a larger and (B) a smaller droplet, both composed of the densest oil mixture ($\rho_d = 0.9927$ g/cm^3) and rising through a 4 cm transition region. The most obvious difference between these two cases is the asymmetry of the droplet's wake. The larger droplet shown in case A, with $\mathrm{Re}_l = 370$, appears to be shedding vortices in a zigzag pattern, while the smaller droplet with $\mathrm{Re}_l = 196$ has a highly symmetric wake structure. This aligns with the delineation of the effect of Reynolds number on the wakes of rising and falling spheres presented in Horowitz & Williamson (2010), who found that in a homogenous fluid, wake structures transition from vertical to oblique at Re = 210, and from oblique to zigzag at Re = 260. The results are also qualitatively very similar to those presented in Hanazaki *et al.* (2009) for spheres in a linear stratification; in our experiments, the finite transition between two homogeneous-density fluids appears to constrain the wake structure to the transition region. While the vortex structures shed by the drop as it leaves the homogeneous lower layer vary between these two experimental cases, they have very similar Froude numbers (0.55 and 0.53), and indeed very similar entrainment times ($t_e = 4.95$ and 4.18 sec; $\tau_e = 29.5$ and 24.9 respectively). This variation in wake structure when entering and initially exiting the transition region thus appears to have little effect on fluid entrainment and drop retention.

Although the far-field wake of the drop seems to have no impact, the gradual bleeding away of the local caudal fluid carried by the drop may instead be the process that governs drop retention. In figures 5 and 6, the width of the tail of fluid dragged by the drop (denoted by changes in ambient illumination in the shadowgraph) slowly decreases over time. Although shadowgraphs are generally a qualitative tool for understanding density variations, we were able to estimate the approximate diameter of the caudal fluid carried by the drop as it rises through and past the transition region. These

values were measured manually for the two cases shown here—as well as three others for which tracking and shadowgraph data were available—approximately one diameter below the bottom of the drop as it rises, as shown in figure 15(a). Because bright and dark regions of the shadowgraph indicate regions of strong concavity in the density field (i.e., large values of $\nabla^2\rho$), actual perturbations in the density field persist slightly farther than can be observed in the shadowgraph. The estimated diameter is thus some fixed fraction of the actual wake diameter; however, we believe this is an adequate analog to examine trends in the wake over time. The ratio of wake diameter to drop diameter is plotted in figure 15(d) versus time nondimensionalized by the buoyancy frequency N. Nondimensionalized position and velocity for each case are also included in (b) and (c) for easy comparison. Time series of wake diameter are shorter than those of tracked position, as the shadowgraphs were zoomed in closer to see fine details and the drop thus remained in the field of view of the camera for a shorter period of time.

An exponential decay can be fit to all five sets of data. Each time series was fit to a function of the form

$$\frac{d_{\text{wake}}}{d} \propto \exp\left(kNt\right), \tag{4.9}$$

yielding an average best-fit decay coefficient of $k = -0.60 \pm 0.06$ across all five cases, with an average R^2 of 0.97. The time at which the drops have asymptoted to their upper-layer terminal velocity, denoted by the vertical colored lines in figure 15, coincides with when the wake diameter is approximately equal to between 1/4 and 1/2 of the drop diameter, indicating that there is less of a wide plume of heavy fluid slowing the droplet by this point in time. The diameter of this caudal fluid then continues to decay with time. This suggests that the trailing fluid may yield an effectively larger frontal area than the drop itself, as shown in the schematic in figure 16. Once the tail has become two to four times smaller than the droplet, the drop reaches its homogeneous upper-layer behavior. These effects could thus be due to both decreased frontal area, as well as the gradual loss of entrained denser fluid.

To our knowledge, this is the first experimental work to quantitatively measure the wake of a spheroid in a density transition, and relate it to the spheroid's slowdown and retention. While these results are preliminary and limited to only a single drop density, we find that this is a promising path to explore further, and hope that a similar approach could further physically motivate the theoretical stratification force drag term studied by Srdić-Mitrović *et al.* (1999), Torres *et al.* (2000), Yick *et al.* (2009) and others.

5. Discussion

5.1. *Implications*

We have studied here the retention and entrainment dynamics of droplets in the regime $0.38 < \text{Fr} < 4.2$, $59 < \text{Re}_l < 1060$, $5.4 < \text{Re}_u < 580$, with relative drop densities $\Delta\rho_u$ ranging from 0.0045 to 0.061, and h/d ranging from 4.5 to 52. Counter to the results of Srdić-Mitrović *et al.* (1999), who found that experiments at higher Re_u (> 15) showed no significant change in drag as a sphere settled through a density gradient, we observed significant drop retention and slowdown for Re_u up to 200, and for a wide range of Re_l. As noted in Abaid *et al.* (2004), the parameters of the layer that a spheroid is entering—in the case of their study and that of Srdić-Mitrović *et al.* (1999), the lower layer layer into which particles were settling—appear to be the most critical for observing "levitation" or significant delay. This holds true in our study, in which a Froude number

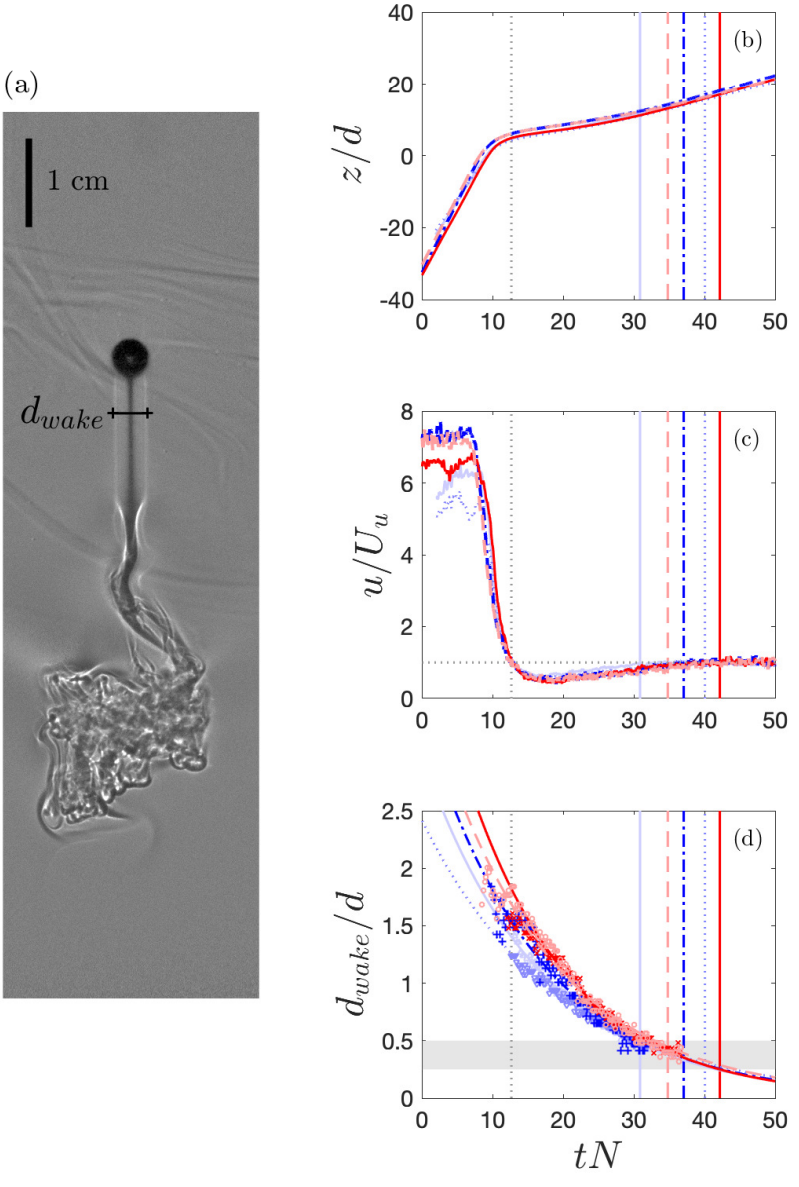

Figure 15: Nondimensionalized tracking and wake diameter data for the shadowgraph experiments shown in figures 5 and 6 (shown in red), as well as three other experiments (shown in blue). Solid red lines correspond to Shadowgraph A, and dashed light red lines correspond to Shadowgraph B. (a) An example of wake diameter measurement. (b,c) Nondimensional drop position and velocity versus time. The vertical dotted grey lines on (b-d) show where the drops first reach U_u; the distances between this and the vertical lines of different shading indicate τ_e for each case. (d) The ratio of drop wake diameter to drop diameter, versus time. For all five cases, values of d_{wake}/d were fit to an exponential curve (lines of corresponding color), yielding a decay coefficient of 0.60±0.06, with an average R^2 of 0.97. Entrainment time approximately corresponds with d_{wake}/d reaching a value between 1/4 and 1/2.

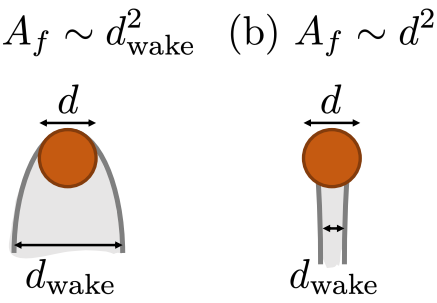

Figure 16: Schematic of drop frontal area A_f (a) during the region of significant drop slowdown, where $d_{wake}/d > 1/2$ and frontal area scales as d^2_{wake}; and (b) after the drop has asymptoted to U_u, where $d_{wake}/d \leqslant 1/2$ and frontal area scales as d^2.

based on the upper layer terminal velocity is the governing parameter. We observed a strong correlation between entrainment and retention timescales and the Froude number, and observed that the diameter of the trailing column of fluid may play an important role in this behavior by governing when the droplet regains its upper-layer velocity. These entrainment and retention effects appear to be independent of the wake dynamics when entering the transition region, which are a function of Re_l.

Beyond oil spills, dynamics explored in this study may also be applicable to natural oil seeps, which account for up to 47% of crude oil entering the marine environment (Kvenvolden & Cooper 2003). Although our results are for liquid droplets in an ambient stratification, we expect some of these findings to hold for solid particles as well, and may have applications in sediment suspension in benthic boundary layers (Adams & Weatherly 1981), sediment plumes entering stratified lakes (Scheu *et al.* 2015), and dispersal of pollutants in the atmosphere (Turco *et al.* 1990).

5.2. *Applicability to the real ocean*

While significant delays were observed in our experiments, these delays only occur for very small Froude numbers ($\mathrm{Fr} \lesssim 1$). On the other hand, the Deepwater Horizon oil spill occurred in an area of the ocean in which the buoyancy frequency N ranged from 0.0004 to 0.0027 s^{-1}. Using a drop diameter of 0.5 cm and a drop velocity of 12 cm/s (Johansen *et al.* 2013), this yields $\mathrm{Fr} \sim 9000$ to 60000, well beyond our retention threshold of $\mathrm{Fr} \lesssim 1$. This suggests that while a single drop is only significantly retained at very low Froude numbers, multiple drops experience different dynamics that allow for the intrusion layers observed following oil well leaks.

We propose that while individual drops in the ocean may not fall below our retention threshold, a bulk plume can have an effective Froude number less than 1. Following Socolofsky & Adams (2005), the characteristic plume velocity is

$$U_c = (BN)^{1/4} \tag{5.1}$$

where B is the kinematic buoyancy flux, defined as $B = gQ(\rho_d - \rho_f)/\rho_f$, and Q is the volumetric flow rate of oil. During the Deepwater Horizon oil spill, volumetric flow rates were about 50,000 to 70,000 barrels per day (McNutt *et al.* 2012). Using Q = 60,000 barrels per day, an ambient oceanic density of $\rho_f = 1027.6$ kg m^{-1} and an oil density of $\rho_d = 858$ kg m^{-1} (Socolofsky *et al.* 2011) the plume velocity was on the order of $U_c = 0.15$ m s^{-1}.

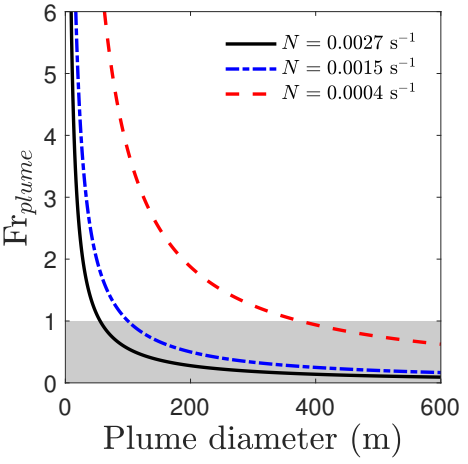

Figure 17: Effective plume Froude number for a range of plume diameters and buoyancy frequencies. The grey shaded region indicates any environmental conditions that would yield a a plume Froude number less than 1.

The effective plume Froude number is thus

$$\mathrm{Fr}_{\mathrm{plume}} = \frac{U_c}{N d_{\mathrm{plume}}}. \tag{5.2}$$

Depending on the ambient stratification, a case of $\mathrm{Fr}_{\mathrm{plume}} < 1$ may occur for a minimum plume diameter of 375 m (N = 0.0004 s^{-1}) to 55 m (N = 0.0027 s^{-1}), as shown in figure 17. In the controlled DeepSpill experiments of Johansen *et al.* (2003), for example, the released plumes had widths on the order of 200-300 meters in an ambient stratification with $N = 0.0015$ s^{-1}, yielding $\mathrm{Fr}_{\mathrm{plume}} \approx 0.4$. Following the Deewpater Horizon spill, the buoyant hydrocarbon plume was observed to surface within a 2 km^2 area (Ryerson *et al.* 2012), giving an estimate of $\mathrm{Fr}_{\mathrm{plume}} = 0.15$ m s^{-1}/(0.0027s^{-1} · 50m) = 1.1. Bulk plume Froude numbers on the order of or less than 1 may thus occur in the field, and further studies involving the extent of fluid entrained by a rising plume would help illuminate this possible explanation.

5.3. *Future directions*

Although our results regarding decay of a droplet's wake are promising, a more systematic study is required to draw stronger conclusions about the relationship between the entrainment timescale and the diameter, length, and overall shape of the trailing fluid column, as well as about the vortex shedding that happens before and during passage through the transition region. We also explored only a certain Froude and Reynolds number regime in this study; it remains to be seen whether this scaling applies to drops that are in the Stokes regime, or for extremely high Reynolds number spheroids, such as rising bubbles.

Finally, we have ignored the role of Marangoni forces in this study. A Marangoni timescale can be derived for a tangential stress balance between viscous stress and the

gradient of interfacial tension. Tam *et al.* (2009) estimated the Marangoni velocity scale as

$$U_M \sim \frac{\partial \gamma}{\partial \rho} \frac{\Delta \rho}{\mu_f}. \tag{5.3}$$

Assuming that the relevant change in density $\Delta\rho$ encountered by a droplet in stratification is $\frac{\partial \rho}{\partial z} d$, this yields a Marangoni timescale of

$$t_{\text{Marangoni}} = \frac{d}{U_M} \approx \frac{\mu_f}{\frac{\partial \gamma}{\partial \rho} \frac{\partial \rho}{\partial z}}. \tag{5.4}$$

In this study, we have not varied the Marangoni timescale in a way that would isolate Marangoni forces from the effects of stratification. Work is currently ongoing to systematically quantify the gradient in interfacial tension a drop might encounter, and whether it is an important timescale in this problem.

6. Conclusions

In this study, we characterized the dynamics behind retention of a single droplet at a transition in density between two homogeneous fluids. We examined fluid flow and droplet retention for a range of drop sizes, drop densities, and ambient stratification profiles, allowing us to characterize drop behavior for a range of Reynolds and Froude numbers.

We explored two metrics measuring the timescale of drop delay at a density transition. The first metric, the entrainment time t_e, measures the amount of time that denser fluid is appreciably entrained, reducing the drop's speed. The second, the retention time t_r, measures the degree to which the droplet's rise is delayed. The retention time is related to the entrainment time by a simple linear relation involving the degree of slowdown the droplet experiences, $t_r = 0.46 t_e (\Delta U / U_u)$.

In the regime covered by our experiments ($0.38 < \text{Fr} < 4.2$, $59 < \text{Re}_l < 1060$, $5.4 < \text{Re}_u < 580$, $0.0045 < \Delta\rho_u < 0.61$), nondimensional entrainment and retention times were found to depend strongly on Froude number, yielding $\tau_e = 14\ \text{Fr}^{-1.1}$ and $\tau_r = 2.2\ \text{Fr}^{-1.9}$. Thus, a drop's retention in the stratified interior is a function of its speed in the upper layer (in turn a function of drop density, fluid density, fluid viscosity, and drop diameter) and the ambient density gradient. In light of the strong relationship between drop Reynolds number and Archimedes number discussed in section 4.2, this suggests that knowing an oil droplet's characteristic size and density and properties of the ambient fluid is enough to predict the degree to which it will be retained at a density interface.

Significant retention with any metric only occurred for $\text{Fr} < 1$, suggesting that retention is primarily a function of the ratio of the buoyancy frequency ($1/N$) to the drop motion timescale (d/U_u), and that trapping dynamics are dominated by the effects of stratification. We also found that the trailing column of dense fluid entrained by a droplet decays over time, and that the point at which the wake diameter becomes on the order of 1/4 to 1/2 of the drop diameter coincides with the drop reaching its upper-layer terminal velocity. This effect appears to be independent of the type of wake (zigzagging or vertical) the droplet has when first entering the transition region.

Given that single droplets in oceanic stratifications have Froude numbers on the order of 1,000-10,000, it is likely that plume (i.e., multi-drop and multiphase) dynamics play an important role in producing drop retention at the higher drop Froude numbers observed in the field. We propose that plumes have an effective bulk Froude number

that, using a bulk plume diameter, can yield effective Froude numbers less than 1, and may explain the trapping of large plumes in the field.

Acknowledgments

S.K. acknowledges support from the Hellman Faculty Fellows Fund. The authors thank Thomas Bellotti and Joshua Roe for contributing to numerous discussions on this project. The cameras used in this study were generously lent by Jian-Qiao Sun. The authors also acknowledge the Joint Applied Math and Marine Sciences Fluids Lab at the University of North Carolina at Chapel Hill, where S.K. was a postdoctoral researcher, including Roberto Camassa, Richard McLaughlin, Holly Arrowood, Lauren Colberg, Elaine Monbureau, Sarah Spivey, and Arthur Wood for contributing to preliminary stages of this project.

REFERENCES

Abaid, N., Adalsteinsson, D., Agyapong, A. & McLaughlin, R. M. 2004 An internal splash: Levitation of falling spheres in stratified fluids. *Physics of Fluids* **16** (5), 1567–1580.

Adalsteinsson, D., Camassa, R., Harenberg, S., Lin, Z., McLaughlin, R. M., Mertens, K., Reis, J., Schlieper, W. & White, B. 2011 Subsurface trapping of oil plumes in stratification: Laboratory investigations. In *Monitoring and Modeling the Deepwater Horizon Oil Spill: A Record-Breaking Enterprise* (ed. Yonggang Liu, Amy MacFadyen, Zhen-Gang Ji & Robert H. Weisberg), *Geophysical Monograph Series*, vol. 195, pp. 257–262. American Geophysical Union.

Adams, C. E. & Weatherly, G. L. 1981 Suspended-sediment transport and benthic boundary-layer dynamics. *Marine Geology* **42** (1), 1–18.

Akiyama, S., Waki, Y., Okino, S. & Hanazaki, H. 2019 Unstable jets generated by a sphere descending in a very strongly stratified fluid. *Journal of Fluid Mechanics* **867**, 26–44.

Alavian, V., Jirka, G. H., Denton, R. A., Johnson, M. C. & Stefan, H. G. 1992 Density Currents Entering Lakes and Reservoirs. *Journal of Hydraulic Engineering* **118** (11), 1464–1489.

Allan, D., Caswell, T., Keim, N. & van der Wel, C. 2016 Trackpy: Trackpy v0.3.2. Zenodo.

Auguste, F. & Magnaudet, J. 2018 Path oscillations and enhanced drag of light rising spheres. *Journal of Fluid Mechanics* **841**, 228–266.

Bäumler, K., Wegener, M., Paschedag, A. R. & Bänsch, E. 2011 Drop rise velocities and fluid dynamic behavior in standard test systems for liquid/liquid extraction—experimental and numerical investigations. *Chemical Engineering Science* **66** (3), 426–439.

Bayareh, M., Dabiri, S. & Ardekani, A. M. 2016 Interaction between two drops ascending in a linearly stratified fluid. *European Journal of Mechanics - B/Fluids* **60**, 127–136.

Bayareh, M., Doostmohammadi, A., Dabiri, S. & Ardekani, A. M. 2013 On the rising motion of a drop in stratified fluids. *Physics of Fluids* **25** (10), 103302.

Bertakis, E., Gross, S., Grande, J., Fortmeier, O., Reusken, A. & Pfennig, A. 2010 Validated simulation of droplet sedimentation with finite-element and level-set methods. *Chemical Engineering Science* **65** (6), 2037–2051.

Blanchette, F. & Shapiro, A. M. 2012 Drops settling in sharp stratification with and without Marangoni effects. *Physics of Fluids* **24** (4), 042104.

Camassa, R., Falcon, C., Lin, J., McLaughlin, R. M. & Mykins, N. 2010 A first-principle predictive theory for a sphere falling through sharply stratified fluid at low Reynolds number. *Journal of Fluid Mechanics* **664**, 436–465.

Camassa, R., Falcon, C., Lin, J., McLaughlin, R. M. & Parker, R. 2009 Prolonged residence times for particles settling through stratified miscible fluids in the Stokes regime. *Physics of Fluids* **21** (3), 031702.

Camassa, R., Khatri, S., McLaughlin, R. M., Prairie, J. C., White, B. L. & Yu, S. 2013 Retention and entrainment effects: Experiments and theory for porous spheres settling in sharply stratified fluids. *Physics of Fluids* **25** (8), 081701.

Camilli, R., Reddy, C. M., Yoerger, D. R., Mooy, B. A. S. V., Jakuba, M. V., Kinsey, J. C., McIntyre, C. P., Sylva, S. P. & Maloney, J. V. 2010 Tracking Hydrocarbon Plume Transport and Biodegradation at Deepwater Horizon. *Science* **330** (6001), 201–204.

Clift, R., Grace, J. R. & Weber, M. E. 2005 *Bubbles, Drops, and Particles*. Courier Corporation.

Dabiri, S., Doostmohammadi, A., Bayareh, M. & Ardekani, A. M. 2015 Rising motion of a swarm of drops in a linearly stratified fluid. *International Journal of Multiphase Flow* **69**, 8–17.

Dalziel, S. B., Hughes, G. O. & Sutherland, B. R. 2000 Whole-field density measurements by 'synthetic schlieren'. *Experiments in Fluids* **28** (4), 322–335.

Ganguly, U. P. 1990 On the prediction of terminal settling velocity of solids in liquid-solid systems. *International Journal of Mineral Processing* **29** (3), 235–247.

Gros, J., Socolofsky, S. A., Dissanayake, A. L., Jun, I., Zhao, L., Boufadel, M. C., Reddy, C. M. & Arey, J. S. 2017 Petroleum dynamics in the sea and influence of subsea dispersant injection during Deepwater Horizon. *Proceedings of the National Academy of Sciences* **114** (38), 10065–10070.

Hanazaki, H., Kashimoto, K. & Okamura, T. 2009 Jets generated by a sphere moving vertically in a stratified fluid. *Journal of Fluid Mechanics* **638**, 173–197.

Horowitz, M. & Williamson, C. H. K. 2010 The effect of Reynolds number on the dynamics and wakes of freely rising and falling spheres. *Journal of Fluid Mechanics* **651**, 251–294.

Johansen, Ø., Brandvik, P. J. & Farooq, U. 2013 Droplet breakup in subsea oil releases – Part 2: Predictions of droplet size distributions with and without injection of chemical dispersants. *Marine Pollution Bulletin* **73** (1), 327–335.

Johansen, Ø., Rye, H. & Cooper, C. 2003 DeepSpill—Field Study of a Simulated Oil and Gas Blowout in Deep Water. *Spill Science & Technology Bulletin* **8** (5), 433–443.

Kessler, J. D., Valentine, D. L., Redmond, M. C., Du, M., Chan, E. W., Mendes, S. D., Quiroz, E. W., Villanueva, C. J., Shusta, S. S., Werra, L. M., Yvon-Lewis, S. A. & Weber, T. C. 2011 A Persistent Oxygen Anomaly Reveals the Fate of Spilled Methane in the Deep Gulf of Mexico. *Science* **331** (6015), 312–315.

Kvenvolden, K. A. & Cooper, C. K. 2003 Natural seepage of crude oil into the marine environment. *Geo-Marine Letters* **23** (3-4), 140–146.

Lam, T., Vincent, L. & Kanso, E. 2019 Passive flight in density-stratified fluids. *Journal of Fluid Mechanics* **860**, 200–223.

McNutt, M. K., Camilli, R., Crone, T. J., Guthrie, G. D., Hsieh, P. A., Ryerson, T. B., Savas, O. & Shaffer, F. 2012 Review of flow rate estimates of the Deepwater Horizon oil spill. *Proceedings of the National Academy of Sciences of the United States of America* **109** (50), 20260–20267.

Mehaddi, R., Candelier, F. & Mehlig, B. 2018 Inertial drag on a sphere settling in a stratified fluid. *Journal of Fluid Mechanics* **855**, 1074–1087.

Murphy, D. W., Xue, X., Sampath, K. & Katz, J. 2016 Crude oil jets in crossflow: Effects of dispersant concentration on plume behavior. *Journal of Geophysical Research: Oceans* **121** (6), 4264–4281.

Okino, S., Akiyama, S. & Hanazaki, H. 2017 Velocity distribution around a sphere descending in a linearly stratified fluid. *Journal of Fluid Mechanics* **826**, 759–780.

Panah, M., Blanchette, F. & Khatri, S. 2017 Simulations of a porous particle settling in a density-stratified ambient fluid. *Physical Review Fluids* **2** (11), 114303.

Prairie, J. C., Ziervogel, K., Arnosti, C., Camassa, R., Falcon, C., Khatri, S., McLaughlin, R. M., White, B. L. & Yu, S. 2013 Delayed settling of marine snow at sharp density transitions driven by fluid entrainment and diffusion-limited retention. *Marine Ecology Progress Series* **487**, 185–200.

Ryerson, T. B., Camilli, R., Kessler, J. D., Kujawinski, E. B., Reddy, C. M., Valentine, D. L., Atlas, E., Blake, D. R., de Gouw, J., Meinardi, S., Parrish, D. D., Peischl, J., Seewald, J. S. & Warneke, C. 2012 Chemical data quantify

Deepwater Horizon hydrocarbon flow rate and environmental distribution. *Proceedings of the National Academy of Sciences* **109** (50), 20246–20253.

Scheu, K. R., Fong, D. A., Monismith, S. G. & Fringer, O. B. 2015 Sediment transport dynamics near a river inflow in a large alpine lake. *Limnology and Oceanography* **60** (4), 1195–1211.

Seol, D.-G., Bryant, D. B. & Socolofsky, S. A. 2009 Measurement of Behavioral Properties of Entrained Ambient Water in a Stratified Bubble Plume. *Journal of Hydraulic Engineering* **135** (11), 983–988.

Settles, G. S. 2012 *Schlieren and Shadowgraph Techniques: Visualizing Phenomena in Transparent Media*. Springer Science & Business Media.

Socolofsky, S. A. & Adams, E. E. 2002 Multi-phase plumes in uniform and stratified crossflow. *Journal of Hydraulic Research* **40** (6), 661–672.

Socolofsky, S. A. & Adams, E. E. 2005 Role of Slip Velocity in the Behavior of Stratified Multiphase Plumes. *Journal of Hydraulic Engineering* **131** (4), 273–282.

Socolofsky, S. A., Adams, E. E. & Sherwood, C. R. 2011 Formation dynamics of subsurface hydrocarbon intrusions following the Deepwater Horizon blowout. *Geophysical Research Letters* **38** (9).

Srdić-Mitrović, A. N., Mohamed, N. A. & Fernando, H. J. S. 1999 Gravitational settling of particles through density interfaces. *Journal of Fluid Mechanics* **381**, 175–198.

Sutherland, B. R., Dalziel, S. B., Hughes, G. O. & Linden, P. F. 1999 Visualization and measurement of internal waves by 'synthetic schlieren'. Part 1. Vertically oscillating cylinder. *Journal of Fluid Mechanics* **390**, 93–126.

Tam, D., von Arnim, V., McKinley, G. H. & Hosoi, A. E. 2009 Marangoni convection in droplets on superhydrophobic surfaces. *Journal of Fluid Mechanics* **624**, 101–123.

Torres, C. R., Hanazaki, H., Ochoa, J., Castillo, J. & Woert, M. V. 2000 Flow past a sphere moving vertically in a stratified diffusive fluid. *Journal of Fluid Mechanics* **417**, 211–236.

Turco, R. P., Toon, O. B., Ackerman, T. P., Pollack, J. B. & Sagan, C. 1990 Climate and smoke: An appraisal of nuclear winter. *Science* **247** (4939), 166–176.

Wallis, G. B. 1974 The terminal speed of single drops or bubbles in an infinite medium. *International Journal of Multiphase Flow* **1** (4), 491–511.

Weber, T. C., Robertis, A. D., Greenaway, S. F., Smith, S., Mayer, L. & Rice, G. 2012 Estimating oil concentration and flow rate with calibrated vessel-mounted acoustic echo sounders. *Proceedings of the National Academy of Sciences* **109** (50), 20240–20245.

Wegener, M., Kraume, M. & Paschedag, A. R. 2010 Terminal and transient drop rise velocity of single toluene droplets in water. *AIChE Journal* **56** (1), 2–10.

Yick, K. Y., Torres, C. R., Peacock, T. & Stocker, R. 2009 Enhanced drag of a sphere settling in a stratified fluid at small Reynolds numbers. *Journal of Fluid Mechanics* **632**, 49–68.